Journal of Medical Ultrasonics (2022) 49:555–567
https://doi.org/10.1007/s10396-022-01243-1

ORIGINAL ARTICLE–PHYSICS & ENGINEERING

Application of low-complexity generalized coherence factor to in vivo data

Masanori Hisatsu[1,2] · **Shohei Mori**[3] · **Mototaka Arakawa**[2,3] · **Hiroshi Kanai**[3,2]

Received: 5 April 2022 / Accepted: 14 June 2022 / Published online: 30 August 2022

Abstract

Purpose Beamforming using the generalized coherence factor (GCF) reduces sidelobe artifacts and provides an excellent contrast-to-noise ratio. We previously proposed GCF_{real}, a method to calculate GCF without generating analytic signals, and GCF_{bin}, a method to calculate GCF by binarizing the received signals. In this study, we applied these methods to in vivo data and showed the effect of the computational complexity reduction on contrast performance.

Methods Channel RF data were acquired from the human liver and gallbladder. We set up several observation points in each data set and investigated the mechanism that causes the differences in contrast performance among the methods based on the signals and their power spectra in the channel direction.

Results For GCF and GCF_{real}, the obtained values were almost the same. However, there were large differences in GCF_{bin} from GCF when the signals from the focus point or from outside the focus point were received on different channels. This is because the amplitudes of the signals with high coherence and those with low coherence were changed by binarizing the signals.

Conclusion While GCF_{bin} can significantly reduce the computational complexity, there are differences in the values of GCF_{bin} and GCF due to binarizing of the received signals. However, this difference resulted in GCF_{bin} being superior to GCF in terms of artifact reduction. This is owing to the elimination of amplitude information in GCF_{bin}, which makes it a new efficient coherence factor with different characteristics from GCF.

Keywords Ultrasound imaging · Adaptive beamforming · Generalized coherence factor · In vivo data

Introduction

In ultrasonography, the contrast performance of ultrasound images is important, because diagnosis is often based on minute changes in brightness between the lesion and normal tissues. In delay-and-sum (DAS) beamforming, which is a standard beamforming technique in medical ultrasound imaging, unnecessary signal components from outside the receiving focus point remain due to sidelobes. These unnecessary signals are displayed as artifacts on the B-mode image and reduce the contrast. Apodization, which weights a preset window function onto the transmitted and received signals of individual elements, is a general method for reducing sidelobe components. However, apodization degrades the lateral resolution and signal-to-noise ratio.

Another factor that reduces the visibility of lesion tissue is speckle [1, 2], which occurs on the B-mode images. Speckle, which is generated by the interference of ultrasound waves from many scatterers, is a variation in the brightness values that are not directly related to the structure of the body. When speckle occurs, the contrast-to-noise ratio (CNR) [3], which indicates contrast performance, decreases, and the visibility of lesion tissue is degraded.

Various adaptive beamforming techniques have been proposed to reduce unnecessary signals in the received signals [4–6]. A beamforming technique based on a coherence factor (CF) [7–14] has been proposed as an effective method to reduce unnecessary signals caused

✉ Masanori Hisatsu
masanori.hisatsu.uc@fujifilm.com

1 FUJIFILM Healthcare Corporation, 3-1-1 Higashikoigakubo, Kokubunji, Tokyo 185-0014, Japan

2 Graduate School of Biomedical Engineering, Tohoku University, Sendai, Miyagi 980-8579, Japan

3 Graduate School of Engineering, Tohoku University, Sendai, Miyagi 980-8579, Japan

by sidelobes with low computational complexity. In this technique, the brightness values of pixels dominated by unnecessary signals are reduced by weighting the signals after DAS with a CF [7, 15, 16], which represents the coherence among the received signals of individual elements. One of the factors, the generalized coherence factor (GCF) [8, 9], focuses on the depiction of diffused scattering media and is superior to other factors in terms of CNR, because it reduces sidelobe artifacts without emphasizing speckle [17].

We previously proposed GCF_{real} [18], a method to calculate GCF values without generating analytic (i.e., IQ) signals for the received signals of individual elements, and GCF_{bin} [19], a method that further reduces the computational complexity of GCF_{real} by binarizing the received signals. We applied GCF_{real} and GCF_{bin} to RF data acquired from phantoms and confirmed that the improvements in contrast performance were equivalent to those of conventional GCF. Compared to GCF, GCF_{bin} is much more feasible to implement in commercial ultrasound systems due to its low computational complexity. However, due to the binarization of the signals, the GCF_{bin} value is different from the conventional GCF value. In this study, we applied these methods to in vivo data of the human liver and gallbladder, and by referring to the signal values (analytical signal, I signal, and binarized signal) in the channel direction and their power spectra, we discussed the mechanism that causes the difference in each method and its effect on the B-mode image.

Materials and methods

Generalized coherence factor estimated from real and binarized signals [18, 19]

Figure 1 shows the system block diagram of the receive beamformer using GCF. The GCF is calculated from the received signal $s(m,n,l)$ after delay processing and before summation and is used as a weighting value for the signal $x_{in}(n,l)$ after applying DAS. Here, $m(m=0,1,\cdots,M-1)$ is the channel number, n is the sample number in the time direction, and l is the scan line number.

In the GCF estimator shown in Fig. 1, the analytic signal is

$$I(m,n,l)+\mathrm{j}Q(m,n,l)=A(m,n,l)\exp\left[\mathrm{j}2\pi fnT\right], \tag{1}$$

which is calculated by the Hilbert transform in the nth direction for $s(m,n,l)$. Here, $A(m,n,l)$ is the complex amplitude, f represents the carrier frequency of the received signal, and T represents the reception sampling period. The GCF value is calculated from Eq. (2) using the $S_{IQ}(k,n,l)$ obtained by the discrete Fourier transform (DFT) in the mth direction for the analytic signals [8]:

$$\begin{aligned} GCF\left(n,l;K_0\right) &= \frac{\sum_{k=-K_0}^{K_0}\left|S_{IQ}(k,n,l)\right|^2}{\sum_{k=-K}^{K-1}\left|S_{IQ}(k,n,l)\right|^2} \\ &= \frac{\sum_{k=-K_0}^{K_0}\left|S_{IQ}(k,n,l)\right|^2}{M\cdot\sum_{m=0}^{M-1}\left|I(m,n,l)+\mathrm{j}Q(m,n,l)\right|^2}, \end{aligned} \tag{2}$$

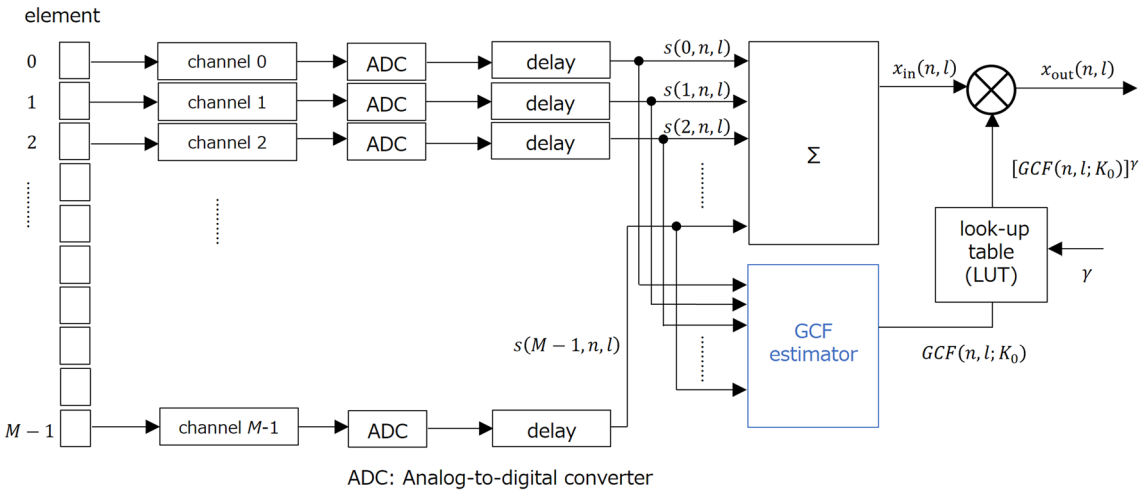

Fig. 1 System block diagram for coherence-weighted beamforming using GCF

where k is the frequency index in the channel direction, and $k = -K, -K+1, \ldots, 0, \ldots, K-1, (K = M/2)$ for an even number M. The GCF value is the ratio of the power value of the frequency component in the range of $[-K_0, K_0]$ (numerator) to the power value of all frequency components (denominator). The above shows the case of using the Hilbert transform, but the same approach can be applied to the case of baseband demodulation.

By weighting the signal $x_{\text{in}}(n,l)$ by the GCF value, $x_{\text{in}}(n,l)$ including unnecessary signals is suppressed. The index $\gamma(>0)$ is used to adjust the effect of the weighting as

$$x_{\text{out}}(n,l) = \left[GCF\left(n,l;K_0\right)\right]^{\gamma} x_{\text{in}}(n,l). \tag{3}$$

Adjustment by the power γ is implemented using a look-up table (LUT), as outlined in Fig. 1. The LUT outputs a tabled $\left[GCF\left(n,l;K_0\right)\right]^{\gamma}$ value for the input $GCF\left(n,l;K_0\right)$ value.

To reduce the computational complexity of calculating GCF values, we proposed GCF_{real}, a method that calculates GCF values from real signals without generating an analytic signal for each channel [18]. The power spectrum of $S(k,n,l)$ obtained by DFT in the mth direction for real signals is expressed by the following equation using $S_{\text{IQ}}(k,n,l)$:

$$\begin{aligned}|S(k,n,l)|^2 &= \left|\frac{1}{2}\left\{S_{\text{IQ}}(k,n,l) + S^*_{\text{IQ}}(-k,n,l)\right\}\right|^2 \\ &= \frac{1}{4}\left\{\left|S_{\text{IQ}}(k,n,l)\right|^2 + S_{\text{IQ}}(k,n,l)S_{\text{IQ}}(-k,n,l) + S^*_{\text{IQ}}(k,n,l)S^*_{\text{IQ}}(-k,n,l) + \left|S^*_{\text{IQ}}(-k,n,l)\right|^2\right\}\end{aligned} \tag{4}$$

Replacing $\left|S_{\text{IQ}}(k,n,l)\right|^2$ in Eq. (2) with $|S(k,n,l)|^2$ in Eq. (4), Eq. (2) can be rewritten as

$$GCF_1\left(n,l;K_0\right) = \frac{\sum_{k=-K_0}^{K_0}\left|S_{\text{IQ}}(k,n,l)\right|^2 + \sum_{k=-K_0}^{K_0}\text{Re}\left[S_{\text{IQ}}(k,n,l)S_{\text{IQ}}(-k,n,l)\right]}{\sum_{k=-K}^{K-1}\left|S_{\text{IQ}}(k,n,l)\right|^2 + \sum_{k=-K}^{K-1}\text{Re}\left[S_{\text{IQ}}(k,n,l)S_{\text{IQ}}(-k,n,l)\right]}. \tag{5}$$

As the first terms in the numerator and denominator of Eq. (5) are the same as those of Eq. (2), they are expressed as GCF terms. Furthermore, $\left|S_{\text{IQ}}(k,n,l)\right|^2$ in the GCF term is expressed as

$$\left|S_{\text{IQ}}(k,n,l)\right|^2 = \frac{1}{M^2}\left|\sum_{m=0}^{M-1} A(m,n,l)\exp\left[-\text{j}\frac{2mk\pi}{M}\right]\right|^2. \tag{6}$$

Thus, the GCF term in the nth direction exhibits a gradual change based on the envelope amplitude $A(m,n,l)$. On the other hand, $S_{\text{IQ}}(k,n,l)S_{\text{IQ}}(-k,n,l)$ in the second term (cross term) of each of the numerator and denominator in Eq. (5) is expressed by

$$\begin{aligned}&S_{\text{IQ}}(k,n,l)S_{\text{IQ}}(-k,n,l) = \\ &\frac{1}{M^2}\exp\left[\text{j}4\pi fnT\right]\sum_{m=0}^{M-1} A(m,n,l)\exp\left[-\text{j}\frac{2mk\pi}{M}\right]\sum_{m=0}^{M-1} A(m,n,l)\exp\left[\text{j}\frac{2mk\pi}{M}\right],\end{aligned} \tag{7}$$

where there is a component of frequency $2f$ in the nth direction. In Eq. (2), replacing the analytic signal $I(m,n,l) + \text{j}Q(m,n,l)$ with the real signal $s(m,n,l)$, and $S_{\text{IQ}}(k,n,l)$ with $S(k,n,l)$, followed by adding low-pass filters (LPFs) to the numerator and denominator in the nth direction for reducing the cross terms, GCF_{real} is expressed as

$$GCF_{\text{real}}\left(n,l;K_0\right) = \frac{\sum_{h=-N_{\text{f}}}^{N_{\text{f}}}\left[f_{\text{LPF}}(h)\cdot\left\{\sum_{k=-K_0}^{K_0}|S(k,n-h,l)|^2\right\}\right]}{\sum_{h=-N_{\text{f}}}^{N_{\text{f}}}\left[f_{\text{LPF}}(h)\cdot\left\{M\sum_{m=0}^{M-1}|s(m,n-h,l)|^2\right\}\right]}. \tag{8}$$

Equation (8) shows the case, where a finite impulse response–low-pass filter (FIR–LPF) with coefficients $f_{\text{LPF}}(h), (h = -N_{\text{f}} \ldots N_{\text{f}})$ is used as the LPF.

To further reduce the amount of computation, the input real signal $s(m,n,l)$ is binarized as

$$u(m,n,l) = \begin{cases} -1 \text{ if } s(m,n,l) < 0 \\ +1 \text{ if } s(m,n,l) \geq 0 \end{cases}. \tag{9}$$

In Eq. (8), by replacing $s(m,n,l)$ with $u(m,n,l)$, and $S(k,n,l)$ with $U(k,n,l)$ obtained by DFT of $u(m,n,l)$, we obtain

$$GCF_{\text{bin}}\left(n,l;K_0\right) = \frac{\sum_{h=-N_f}^{N_f}\left[f_{\text{LPF}}(h)\cdot\left\{\sum_{k=-K_0}^{K_0}|U(k,n-h,l)|^2\right\}\right]}{M^2}. \tag{10}$$

Compared with the GCF in Eq. (2), the number of multiplications and additions in GCF_{bin} is greatly reduced [19].

Experimental setup

The experimental RF data were collected from the liver and gallbladder of a 33-year-old healthy male using ultrasonic diagnostic system ProSound α10 (Aloka, Tokyo, Japan) with a convex probe (UST-9130, center frequency 3.5 MHz, radius of curvature 60 mm). In this study, the transmit center frequency was set at 3.5 MHz, and the depth of the transmitting focus

was 105 mm. The echo signals were received by 96 channels, and the RF data were sampled at a sampling frequency of 20 MHz. The number of scan lines of the images was 210 and 312 for the liver and gallbladder data, respectively. As in a previous study [19], we set the channel number to $M = 96$, the DC vicinity range to $K_0 = 1$, and the LPF order to $2N_f = 20$. Under this condition, the number of multiplications of GCF_{bin} was less than 1/100 of that of GCF.

GCF weighting can reduce sidelobe artifacts without speckle enhancement. However, dark region artifacts [20] are generated around strong scatterers. For the liver data, we selected an image in which sidelobe artifacts and dark region artifacts were generated by the diaphragm, which was a strong scatterer. For the gallbladder data, we selected an image that included the homogeneous part of the liver and the hypoechoic part of the gallbladder so that contrast performance could be evaluated. This study was approved by the institutional ethical committee and was performed with the informed consent of the subject.

Figure 2a, b shows the B-mode images of the liver and gallbladder obtained with DAS, respectively. The dynamic range of the display was 80 dB. The sidelobe artifact generated by the diaphragm is indicated by the arrow in Fig. 2a. Figure 2c, d shows the scan line data before scan conversion. The horizontal axis shows the scan line number, and the vertical axis shows the depth. The red points, from A to E, indicate the points, where the signals were observed. At these points, we investigated the mechanism that causes the difference between the methods by observing the signals (analytic signal, I-signal, and binarized signal) in the channel direction used to calculate the GCF in Eq. (2), the GCF_{real} in Eq. (8), and the GCF_{bin} in Eq. (10). Since the purpose was to investigate the difference in methods, it did not matter if the depths of the observation points were different.

Results

Differences of GCF_{real} from GCF and of GCF_{bin} from GCF

Figure 3a, b shows the differences of GCF_{real} values from GCF values:

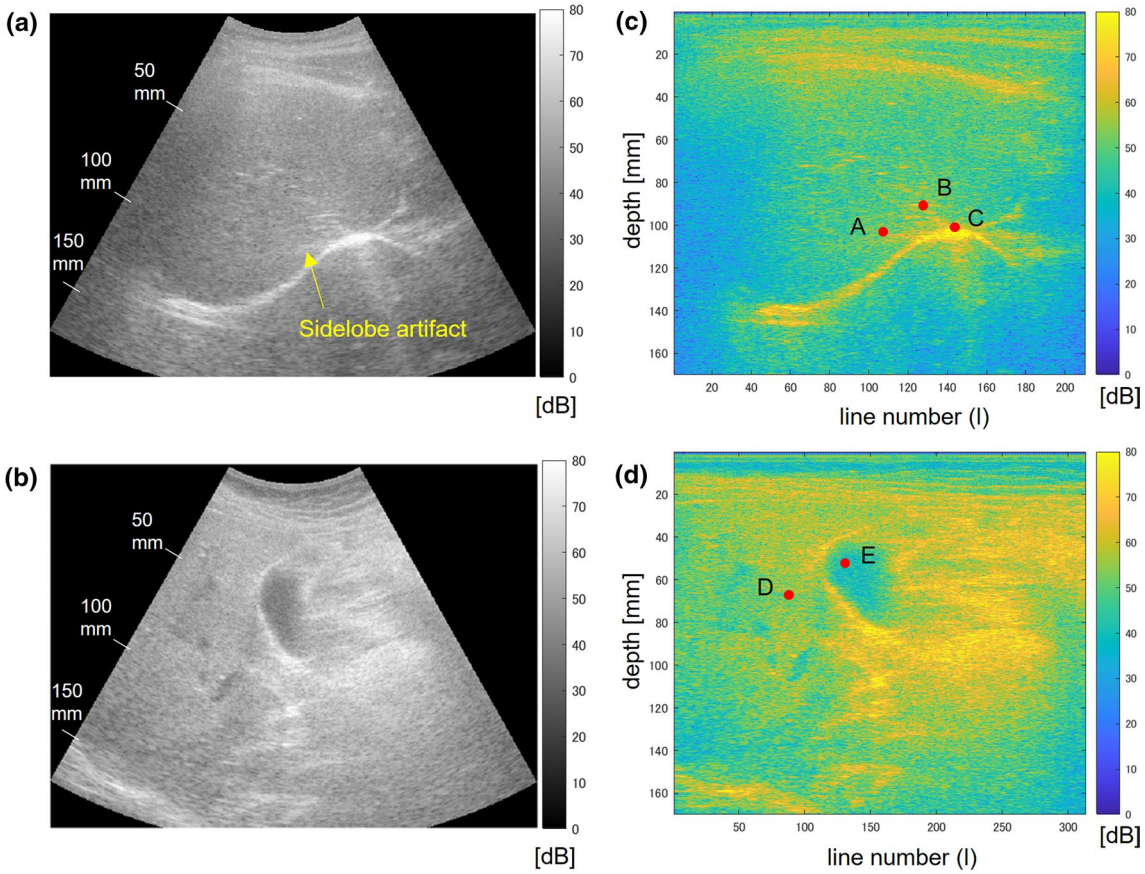

Fig. 2 B-mode images of **a** liver and **b** gallbladder. Scanline data before scan conversion of **c** liver and **d** gallbladder data

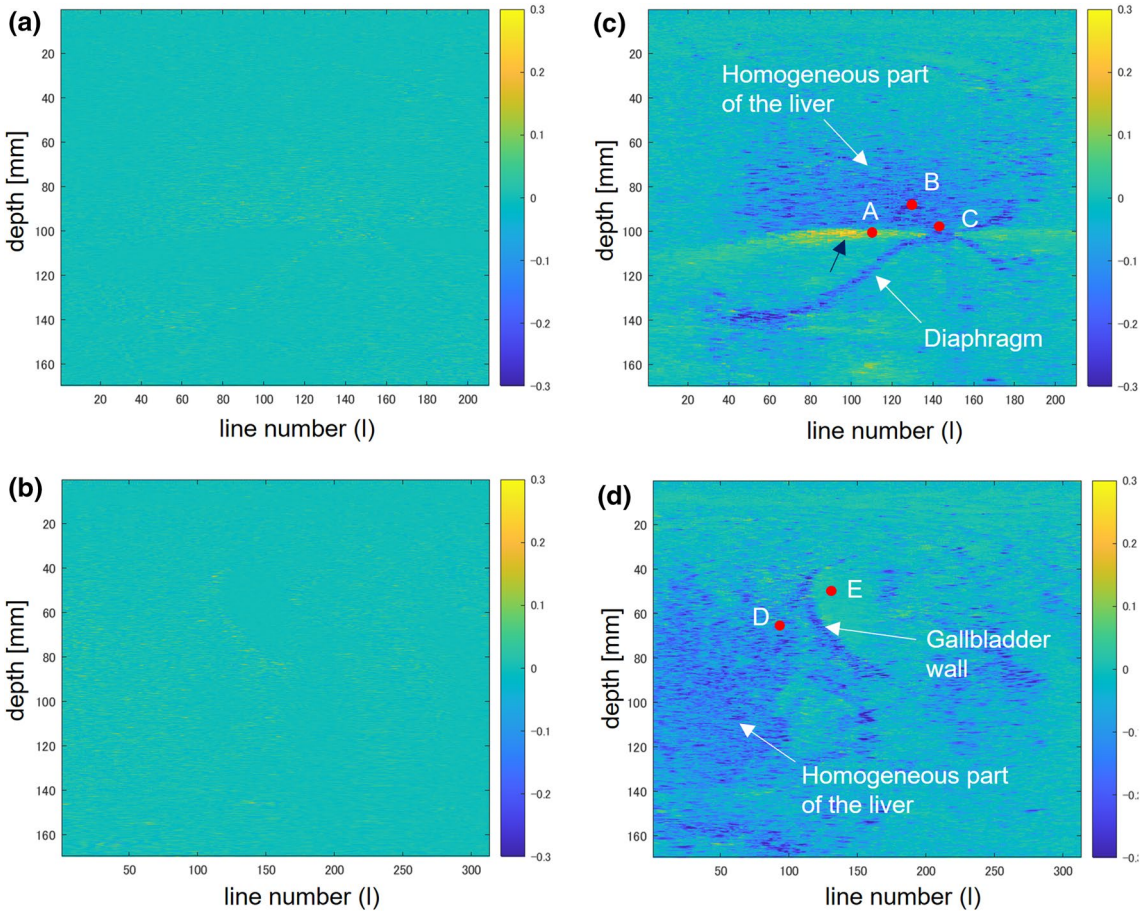

Fig. 3 Difference of GCF_{real} from GCF in **a** liver and **b** gallbladder data. Difference of GCF_{bin} from GCF in **c** liver and **d** gallbladder data

$$\Delta GCF_{\text{real}}(n,l;K_0) = GCF_{\text{real}}(n,l;K_0) - GCF(n,l;K_0), \tag{11}$$

and Fig. 3c, d shows the differences of GCF_{bin} values from GCF values:

$$\Delta GCF_{\text{bin}}(n,l;K_0) = GCF_{\text{bin}}(n,l;K_0) - GCF(n,l;K_0), \tag{12}$$

estimated from the liver and gallbladder data shown in Fig. 2. Here, as in Fig. 2c, d, the data are displayed using the scanning line data before scan conversion.

$\Delta GCF_{\text{bin}}(n,l;1)$ was larger than $\Delta GCF_{\text{real}}(n,l;1)$. In Fig. 3c, d, $\Delta GCF_{\text{bin}}(n,l;1)$ was negative in structures, such as the diaphragm and gallbladder wall, as well as in the homogeneous part of the liver; thus, the GCF_{bin} values were smaller than the GCF values in these areas. In the area shown with the black arrow in Fig. 3c, because $\Delta GCF_{\text{bin}}(n,l;1)$ was positive, GCF_{bin} values were larger than GCF values. For such characteristic positions, the points of interest from A to E, indicated by the red dots, were set. In Figs. 2c and 3c, A represents the homogeneous part of the liver, where $\Delta GCF_{\text{bin}}(n,l;1)$ was a positive value. B represents the position, where the blood vessel wall existed in the homogeneous part of the liver and $\Delta GCF_{\text{bin}}(n,l;1)$ was large on the negative side. C represents the position of the strong scatterer on the diaphragm. In Figs. 2d and 3d, D represents the homogeneous part of the liver, and E represents the hypoechoic region in the gallbladder.

Signals in channel direction and their frequency spectra

The signals after delay processing in the channel direction at point A are shown in Fig. 4a1. Three signals are shown: the I (in-phase) signal, the Q (quadrature-phase) signal, and the binarized signal for the I signal. The GCF value is the ratio of the power value in the vicinity of DC to the total power value; thus, the GCF value does not change even if the amplitude value of the signal is normalized. Therefore, here, the amplitude value of the binarized signal was normalized and displayed so that the total power value was the same as the I signal. When the channel number m was larger than 60,

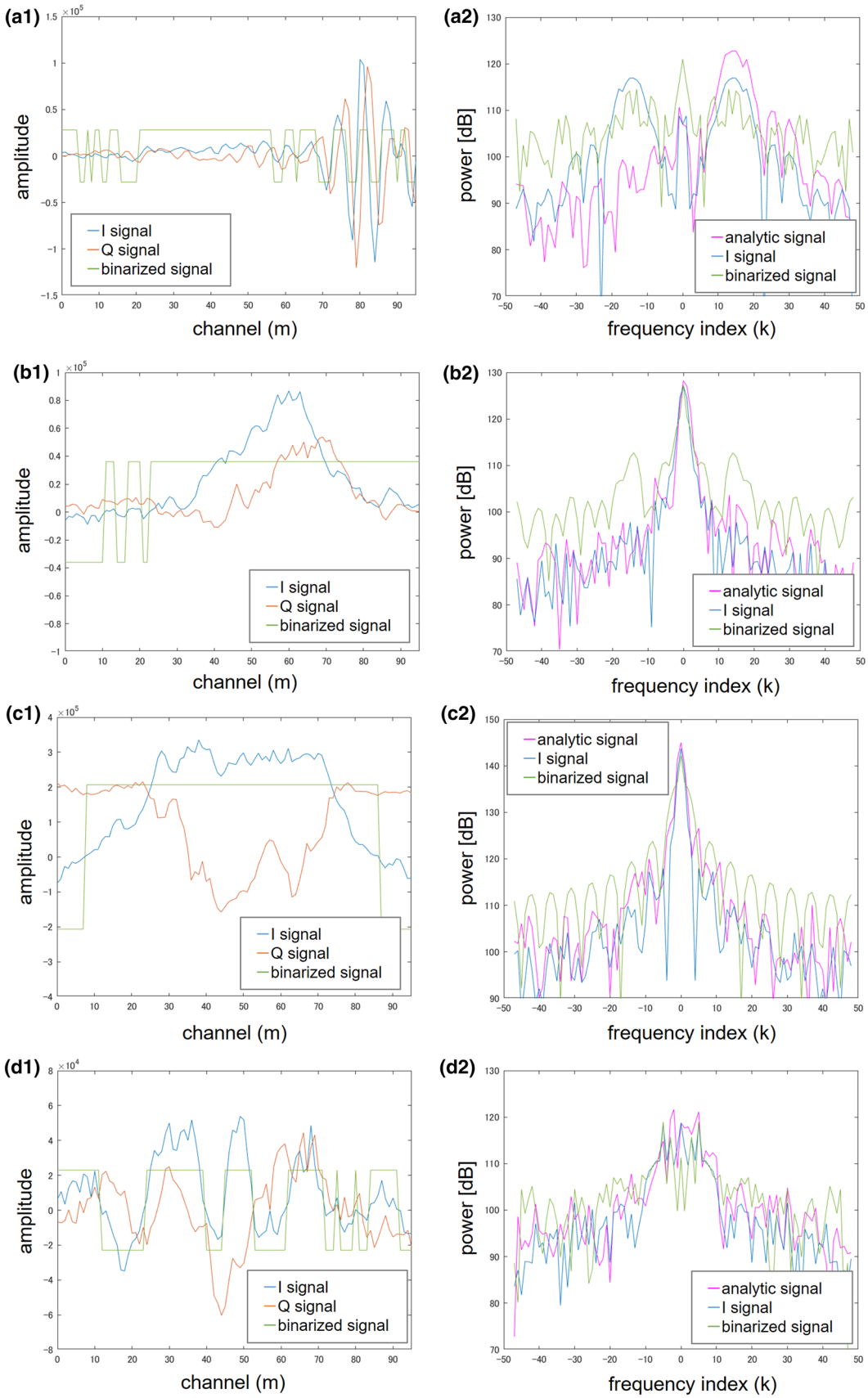

Fig. 4 **a1**–**e1** Signals in the channel direction and **a2**–**e2** their frequency spectra at each observation point indicated by A to E

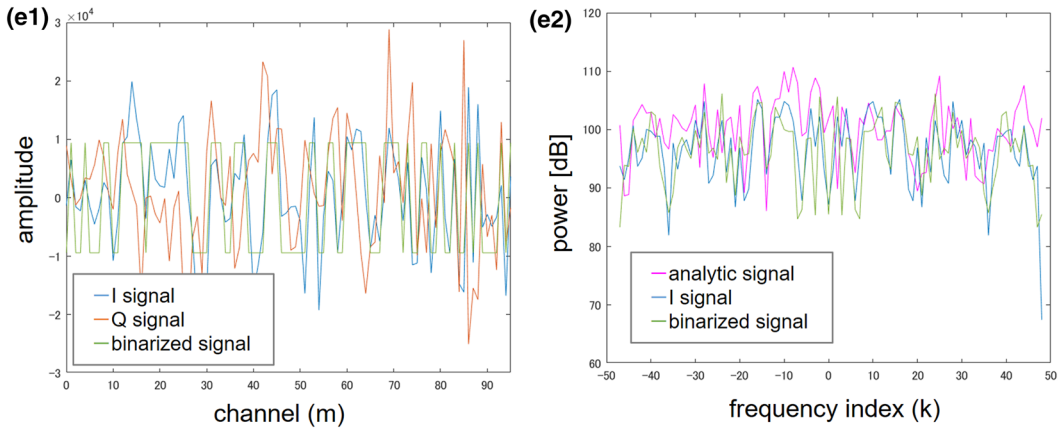

Fig. 4 (continued)

the signals from the strong scatterer at point C were mixed, and the amplitude value of the I and Q signals became high.

Figure 4a2 shows the frequency spectra obtained with DFT in the channel direction for the signals in Fig. 4a1. GCF is calculated from the spectrum of the analytic signals, GCF_{real} is calculated from the spectrum of the I signals, and GCF_{bin} is calculated from the spectrum of the binarized signals. In the spectrum of the analytic signals, the frequency component was large near $k = 15$, and this component was from the strong scatterer at point C. In the spectrum of the binarized signals, the frequency component (around $k = \pm 15$) due to the strong scatterer decreased and the component in the vicinity of DC increased compared to the spectrum of the I signals. Consequently, the values of GCF, GCF_{real}, and GCF_{bin} were 0.01, 0.01, and 0.21, respectively, which showed that GCF_{bin} was larger than GCF and GCF_{real}.

Figure 4b1 shows the received signals at point B. The amplitude values were high at channel numbers 30 to 80, and the fluctuation was gradual. As the signals in this part were dominant, in the frequency spectrum shown in Fig. 4b2, the frequency component was concentrated in the vicinity of DC in each signal. However, because the amplitude value is not considered in the binarized signal, the influence of the signals at $m < 30$ whose amplitude was small and the sign changes became large, and the high-frequency component increased. Consequently, the values of GCF, GCF_{real}, and GCF_{bin} were 0.84, 0.84, and 0.55, respectively, showing that GCF_{bin} was smaller than GCF and GCF_{real}.

Figure 4c1 shows the signals in the channel direction at point C of the strong scatterer of the diaphragm. The coherence of the signals was high, and the frequency spectrum of each signal was concentrated in the vicinity of DC, as shown in Fig. 4c2. However, because of the generation of high-frequency components due to binarization, the values of GCF, GCF_{real}, and GCF_{bin} were 0.91, 0.90, and 0.79, respectively, and only GCF_{bin} was smaller.

Figure 4d1 shows the signals at point D in the liver homogeneous part in the gallbladder data. The IQ signals showed a gradual change in the channel direction. Figure 4d2 shows these frequency spectra, which depicted that the frequency component was distributed in the vicinity of DC in each signal. In addition, as demonstrated in Fig. 4c2, the high-frequency component was increased as a result of binarization. Consequently, the values of GCF, GCF_{real}, and GCF_{bin} were 0.31, 0.31, and 0.23, respectively, and only GCF_{bin} was smaller.

Point E in the hypoechoic region in the gallbladder was a position, where signals from surrounding structures such as the gallbladder wall were mixed. As demonstrated in Fig. 4e1, signals fluctuated drastically in the channel direction due to the scattered waves from the surrounding structures. As shown in Fig. 4e2, the frequency spectrum of each signal was like white noise, and the ratio of the power value in the vicinity of DC to the total power value was small. The values of GCF, GCF_{real}, and GCF_{bin} were as small as 0.02, 0.02, and 0.03, respectively, and the differences among each method were also small.

B-mode images weighted by each method

B-mode images weighted by GCF, GCF_{real}, and GCF_{bin} for the liver data are shown in Fig. 5a–c, and those for the gallbladder data are shown in Figs. 5d–f. The dynamic range was set to 80 dB, as in Fig. 2a, b. For each of GCF, GCF_{real}, and GCF_{bin}, the values $\gamma_{GCF} = 0.2$, $\gamma_{real} = 0.2$, $\gamma_{bin} = 0.26$ adjusted by phantom data [18, 19] were used as the adjustment coefficient γ in Eq. (3). These γ values were adjusted so that the average brightness value of the dark region artifact [20] generated by the strong scatterer of the phantom was the same for each method. The B-mode images weighted by

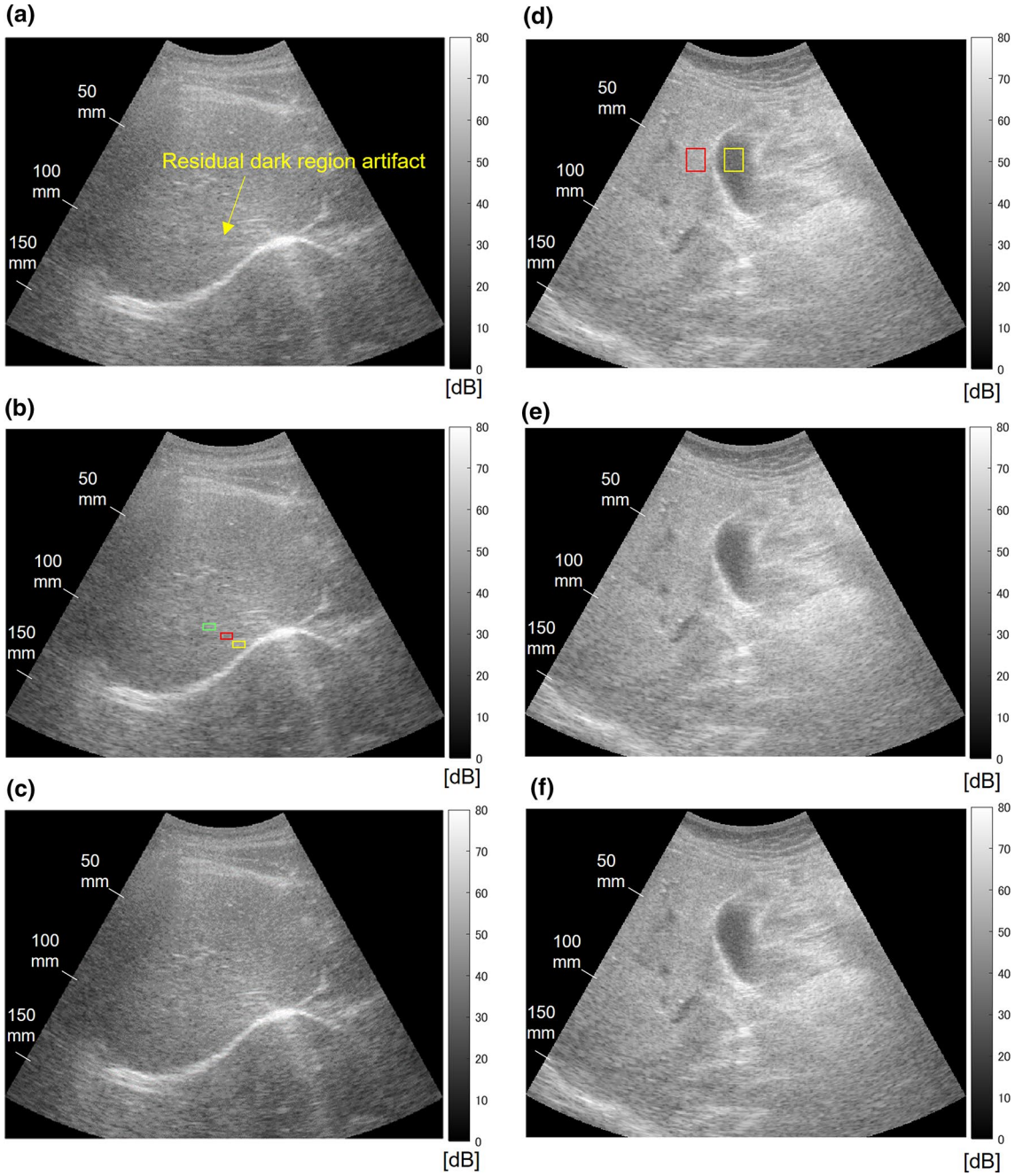

Fig. 5 B-mode images weighted by **a**, **d** GCF, **b**, **e** GCF_{real}, and **c**, **f** GCF_{bin}

GCF and GCF_{real} were almost the same. In the liver data, the dark region artifact generated by the diaphragm, indicated by the arrow in Fig. 5a, remained in GCF and GCF_{real}, but it was not recognizable in GCF_{bin} (Fig. 5c).

For the regions of interest indicated by the squares in Fig. 5b and d, the contrast and CNR [3] values were calculated using

$$Contrast = \mu_1 - \mu_2, \tag{13}$$

$$CNR = \frac{|\mu_1 - \mu_2|}{\sqrt{{\sigma_1}^2 + {\sigma_2}^2}}. \tag{14}$$

Table 1 Contrast values of the sidelobe artifact part concerning the homogeneous part of the liver

	DAS	GCF	GCF_{real}	GCF_{bin}
Contrast [dB]	8.23	4.76	4.72	3.81

Here, μ_i and σ_i are the mean and standard deviation of the envelope signal after log compression in region i. Table 1 shows the contrast values of the sidelobe artifact part (yellow) concerning the homogeneous part (green) shown in Fig. 5b. The larger the value, the stronger the sidelobe artifact. It can be seen that GCF_{bin} reduced sidelobe artifact the most. Table 2 shows the contrast values of the dark region artifact part (red) concerning the homogeneous part (green) shown in Fig. 5b. The smaller the value, the stronger the dark region artifact. In GCF and GCF_{real}, the brightness of the dark region artifact part was greatly reduced compared to DAS, which did not generate an artifact. It can be seen that this decrease in brightness was alleviated with GCF_{bin}. Table 3 shows the contrast and CNR values of the hypoechoic part (yellow) of the gallbladder concerning the homogeneous part (red) shown in Fig. 5d. GCF_{bin} had the same or better contrast performance improvement effect than GCF and GCF_{real}.

Discussion

Spectra of real signals and GCF_{real} values

As mentioned above, GCF and GCF_{real} values were almost the same, and the contrast performance of the B-mode images, shown in Table 1, was also the same. Here, we considered the power spectrum of the analytic signals used to calculate GCF and that of the I signals used to calculate GCF_{real}. Because the kth component of the power spectrum of the I signals is calculated from the $\pm k$th components of the power spectrum of the analytic signals from Eq. (4), the power spectrum of the I signals has a positive–negative symmetry. Assuming that $S_{IQ}(k,n,l)S_{IQ}(-k,n,l)$ and $S_{IQ}{}^{*}(k,n,l)S_{IQ}{}^{*}(-k,n,l)$, which are the components of the cross term, are removed by the LPF in the nth direction in GCF_{real}, the kth component of the power spectrum of the I signals is expressed by

Table 2 Contrast values of the dark region artifact part concerning the homogeneous part of the liver

	DAS	GCF	GCF_{real}	GCF_{bin}
Contrast [dB]	1.46	− 4.83	− 4.77	− 1.14

Table 3 Contrast and CNR values of the hypoechoic part of the gallbladder concerning the homogeneous part of the liver

	DAS	GCF	GCF_{real}	GCF_{bin}
Contrast [dB]	− 15.74	− 19.79	− 19.79	− 20.26
CNR	3.11	3.57	3.58	3.67

$$|S(k,n,l)|^2 = \frac{1}{4}\left\{\left|S_{IQ}(k,n,l)\right|^2 + \left|S_{IQ}{}^{*}(-k,n,l)\right|^2\right\}. \quad (15)$$

Therefore, the kth component of the power spectrum of the I signals is the average value of the $\pm k$ components of the power spectrum of the analytic signals [because Eq. (15) is the power value of the I signal only, which is half the power value of the analytic (IQ) signal, it is multiplied by 1/4]. As shown in the example in the schematic diagram in Fig. 6a2, when there is a frequency component at the frequency k' in the power spectrum of the analytic signals, the frequency component is distributed to $\pm k'$ in the power spectrum of the I signals. Therefore, the GCF_{real} value calculated from the power values in the positive–negative symmetry range $\left[-K_0, K_0\right]$ in the power spectrum of the I signals is equivalent to the GCF value.

Spectra of binarized signals and the mechanism that causes the difference of GCF_{bin} from GCF values

From the power spectrum of the analytic signals and that of the binarized signals, the difference between the GCF_{bin} value and the GCF value is discussed below for each point of interest.

In the case of the analytic signals at point A shown in Fig. 4a1, the signals from the strong scatterer were dominant in some channels, and the signals from the diffused scattering medium, which was the receiving focus point, were dominant in other channels. It can be abstracted as signals with low coherence and signals with high coherence, respectively. The schematic diagram is shown in Fig. 6a1. Let $m_c (0 < m_c < M)$ be the number of channels that receive the high-coherence signals and let the amplitude (absolute value) of the analytic signals be a constant value A_{co}. The remaining channels $(M - m_c)$ receive the signals with low coherence, and amplitude A_{in} is larger than that of A_{co} $(A_{co}/A_{in} \ll 1)$. Figure 6a2 shows a schematic diagram of the frequency spectra obtained with DFT of the signals in the channel direction. Here, the total power value of each spectrum is the same. In the case of the analytic signals shown in Fig. 6a1, the frequency component with high coherence is concentrated in the vicinity of DC, but the power value is small, because the amplitude of the analytic signals is small. The frequency component of the low-coherence part is distributed in the vicinity of the high-frequency $k = k'(> K_0)$

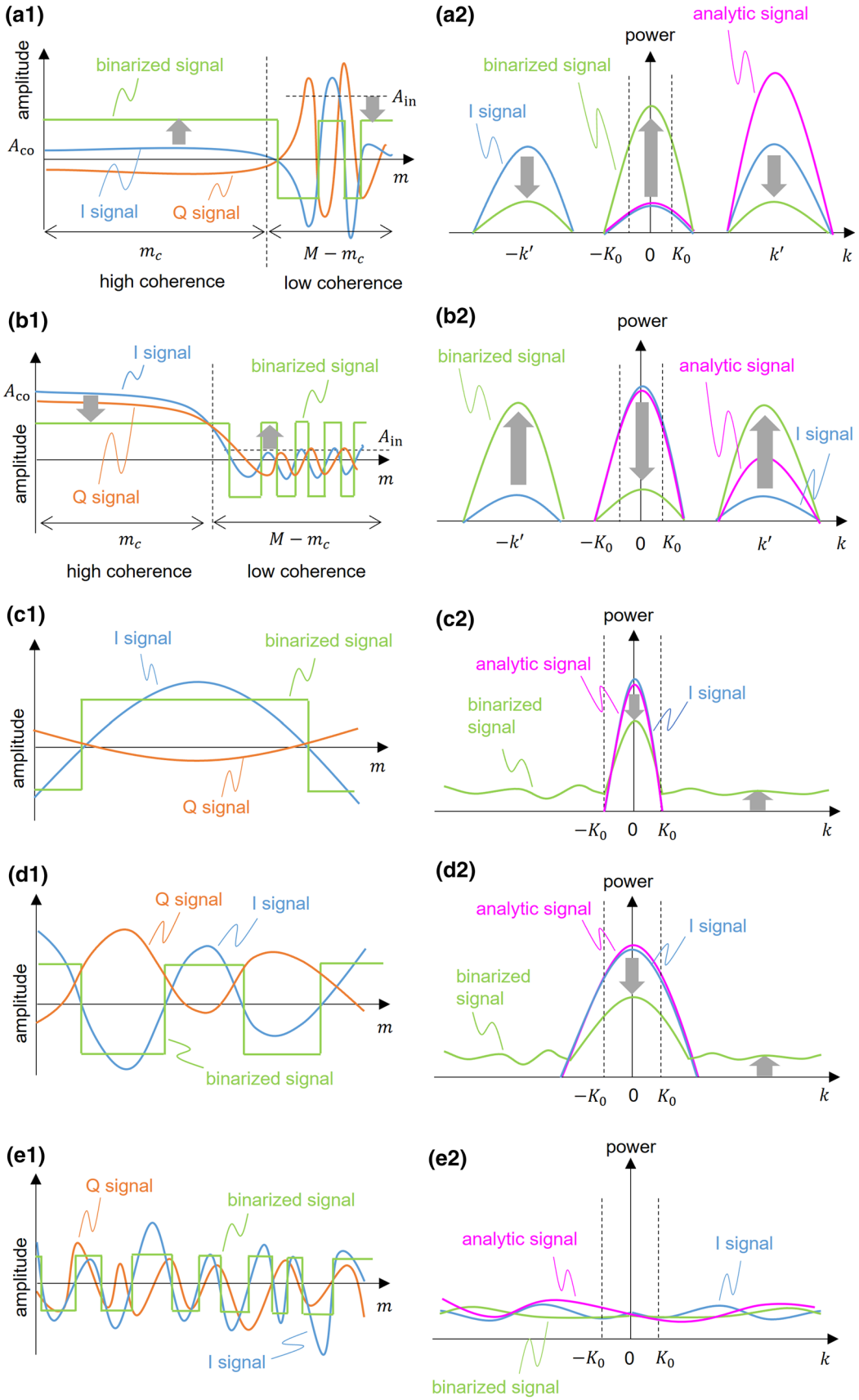

Fig. 6 Schematic diagrams of **a1**–**e1** the signals in the channel direction and **a2**–**e2** their frequency spectra at each observation point indicated by A to E

($k = \pm k'$ in the case of the I signal). Because the amplitude of the analytic signals with low coherence is high, its power value is large. Therefore, GCF and GCF_{real} values are small. On the other hand, in Fig. 6a1, the amplitude of the signals with high coherence becomes relatively large, and that with low coherence becomes relatively small, due to binarization. In addition, in the power spectrum of Fig. 6a2, the GCF_{bin} value becomes larger than the GCF and GCF_{real} values due to the increase in the power value in the vicinity of DC.

At point B, signals with high coherence and signals with low coherence were mixed and received on different channels, as at point A, but as shown in Fig. 6b1, the relationship of the amplitude is the opposite ($A_{in}/A_{co} \ll 1$). In this case, as the amplitude A_{co} of the signals with high coherence is larger than the amplitude A_{in} of the signals with low coherence in the analytic signals and I signals, the power value in the vicinity of DC is also larger than the power value of the signals with low coherence in the vicinity of $k = k'(> K_0)$ ($k = \pm k'$ in the case of the I signal) in the power spectrum, as shown in Fig. 6b2. However, contrary to point A, the amplitude of the signals with high coherence becomes relatively small, and that of the signals with low coherence becomes relatively large, due to binarization. Therefore, the power value of the DC vicinity component becomes smaller, and GCF_{bin} becomes smaller than GCF and GCF_{real}. In this case, since the signal from the focus point is dominant, the brightness should not be reduced. Therefore, the smaller value of GCF_{bin} than GCF is a disadvantage of GCF_{bin}.

The signals at points A and B have different amplitudes for signals with high coherence and signals with low coherence, and they are received by different channels. As a result, GCF_{bin} is significantly different from GCF and GCF_{real}. On the other hand, points C to E, which receive signals from the same source on all channels, are shown below.

In the case of the received signals at points C and D, although there were differences in the channel direction changes and the bandwidth of the power spectrum, the frequency components were concentrated in the vicinity of DC in both cases. Figure 6c1, d1 shows schematic diagrams of the received signals at points C and D, and Fig. 6c2, d2 shows schematic diagrams of their power spectra. Most of the frequency components generated by binarization are considered to appear at $|k| > K_0$, because K_0 is a small number ($K_0 = 1$ in this study). As a result, the ratio of the power value of the DC vicinity component to the total power value decreases, and the GCF_{bin} value decreases compared to the GCF and GCF_{real} values.

Figure 6e1, e2 shows schematic diagrams of the received signals at point E. In the case of the received signals, the signals from the focus point are small, and the signals from outside the focus point are dominant. With respect to the analytic signals and I signals, the ratio of the frequency component of $|k| \le K_0$ is small. Even if high-frequency components are generated by binarization, the change in the power value of $|k| \le K_0$ is small, and the change in the GCF_{bin} value from the GCF value is small. Similarly, when the noise component is dominant due to attenuation, both GCF and GCF_{bin} are small due to the high-frequency components [19].

Advantages of GCF_{bin} over GCF

The GCF value is determined by the ratio of the frequency components of $|k| \le K_0$ and $|k| > K_0$. In general, the received signals contain both of these frequency components. However, there are cases, where all channels contain these components in the same way, such as points C to E, and cases, where each component is received by different channels, such as points A and B. In this paper, the received signals are classified into these patterns, and points A–E are selected. In the case of points C to E, the GCF_{bin} value changes for the GCF value due to the increase in the high-frequency components due to binarization. On the other hand, in the case of points A and B, the dominant signal changes due to binarization, so the change in the GCF_{bin} value for the GCF value tends to be large. This case is considered below.

Signals like those in Fig. 6a1 are generated when there is a scatterer at the receiving focus point, and the received signals from this point are in phase in some channels, but strong signals from outside the focus point are mixed in the other channels. For such received signals, the GCF value is small, and weighting with GCF excessively reduces the signal after DAS and causes dark region artifacts [20] around the strong scatterer. The dark region artifacts caused by the diaphragm's strong scatterer are confirmed in Fig. 5a, b. This artifact is a problem associated with conventional GCF. As shown in Fig. 5c, because the value of GCF_{bin} becomes larger than that of GCF and GCF_{real} in such a region, the artifacts are not noticeable.

Next, consider the signal in Fig. 6b1. Such received signals are generated when the amplitude of the signals from the receiving focus point is large but the signals are not received in some channels. For example, it is thought to occur in the following situations: (1) when the directivity of the reflected wave is strong due to a continuous structure, such as a blood vessel wall, as in the example of point B; (2) when there is a structure in which sound waves do not propagate partially between the receiving focus point and the probe; and (3) when the surface of the probe does not partially touch the body. These phenomena can occur even in ordinary examinations. In such situations, the application of GCF_{bin} may reduce the signal from the receiving focus point compared to GCF. On the other hand, sidelobe

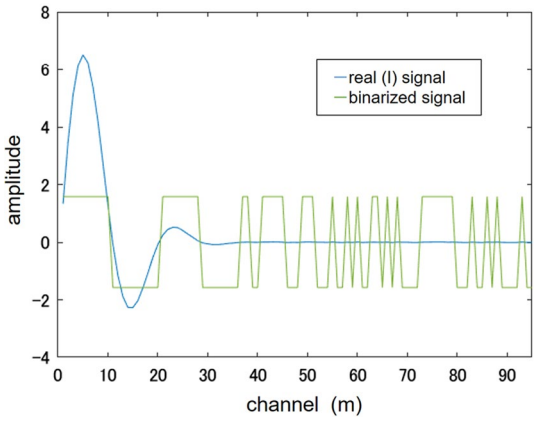

Fig. 7 Example of received signals at the position affected by the sidelobe

artifacts occur when the signals from the scatterer outside the focus point are cut off at the edge of the receiving aperture (channel), as shown in Fig. 7, and the DC component becomes large. Such received signals also correspond to the case of Fig. 6b1, and because GCF_{bin} becomes a smaller value than GCF, it is considered that the sidelobe artifact reduction effect of GCF_{bin} is superior. In this way, even with the same signal pattern, there are cases, where it is desirable to maintain brightness and where it is preferable to reduce it, depending on the target. Distinguishing them is one of the challenges of beamforming using coherence factors.

From the above, as dark region artifacts are less likely to occur with GCF_{bin}, the γ value can be adjusted to further reduce unnecessary signals compared to GCF. This is an advantage of GCF_{bin}. Furthermore, the effect of reducing sidelobe artifacts with GCF_{bin} is higher than that with GCF thanks to binarization. Due to these effects, it can be confirmed from Tables 1 and 2 that GCF_{bin} suppresses dark region artifacts and reduces sidelobe artifacts more than GCF. In addition, it is considered that the effect of improving the contrast between the homogeneous part of the liver and the hypoechoic part of the gallbladder was slightly superior to that of the conventional GCF, as shown in Table 3. Thus, although GCF_{bin} reduced the computational complexity by virtue of binarization of the signal, it was found that the image quality of B-mode images was superior to that of the conventional GCF. It is considered that this is because GCF_{bin} is calculated only from phase information by removing amplitude information, while GCF is calculated from phase and amplitude information. Therefore, GCF_{bin} is considered to be a new coherence factor that not only reduces the computational complexity of GCF but also has different characteristics than GCF.

Conclusion

In this study, targeting signals in the channel direction and their frequency spectra from in vivo data, we considered the mechanism that causes the differences between GCF_{bin}, which reduces the computational complexity of GCF, and GCF.

While GCF and GCF_{real} are coherence factors that include the amplitude values of the signals, the amplitude information disappears due to binarization of the signals with GCF_{bin}. Therefore, the GCF_{bin} value is different from the GCF value. However, owing to this difference, GCF_{bin} may be superior in terms of the ability to reduce artifacts. By removing the amplitude information, GCF_{bin} can be considered a new coherence factor with different characteristics from GCF.

Declarations

Conflict of interest The authors declare that they have no conflicts of interest.

Ethical approval This study was approved by the institutional ethical committee and was performed with the informed consent of the subject.

References

1. Burckhardt CB. Speckle in ultrasound B-mode scans. IEEE Trans Son Ultrason. 1978;25:1–6.
2. Wagner RF, Smith SW, Sandrik JM, et al. Statistics of speckle in ultrasound B-scans. IEEE Trans Son Ultrason. 1983;30:156–63.
3. Patterson MS, Foster FS. The improvement and quantitative assessment of B-mode images produced by an annular array/cone hybrid. Ultrason Imag. 1983;5:195–213.
4. Capon J. High-resolution frequency-wavenumber spectrum analysis. Proc IEEE. 1969;57:1408–18.
5. Synnevag JF, Austeng A, Holm S. Adaptive beamforming applied to medical ultrasound imaging. IEEE Trans Ultrason Ferroelectr Freq Control. 2007;54:1606–13.
6. Synnevag JF, Austeng A, Holm S. Benefits of minimum-variance beamforming in medical ultrasound imaging. IEEE Trans Ultrason Ferroelectr Freq Control. 2009;56:1868–79.
7. Hollman KW, Rigby KW, O'Donnell M. Coherence factor of speckle from a multi-row probe. Proc IEEE Ultrason Symp. 1999;2:1257–60.
8. Li PC, Li ML. Adaptive imaging using the generalized coherence factor. IEEE Trans Ultrason Ferroelectr Freq Control. 2003;50:128–41.
9. Wang SL, Chang CH, Yang HC, et al. Performance evaluation of coherence-based adaptive imaging using clinical breast data. IEEE Trans Ultrason Ferroelectr Freq Control. 2007;54:1669–78.
10. Camacho J, Parrilla M, Fritsch C. Phase coherence imaging. IEEE Trans Ultrason Ferroelectr Freq Control. 2009;56:958–74.

11. Wang Y, Zheng C, Peng H, et al. An adaptive beamforming method for ultrasound imaging based on the mean to standard deviation factor. Ultrasonics. 2018;90:32–41.
12. Hasegawa H, Kanai H. Effect of sub-aperture beamforming on phase coherence factor imaging. IEEE Trans Ultrason Ferroelectr Freq Control. 2014;61:1779–90.
13. Sakhaei SM. Optimum beamforming for sidelobe reduction in ultrasound imaging. IEEE Trans Ultrason Ferroelectr Freq Control. 2012;59:799–805.
14. Nilsen CIC, Holm S. Wiener beamforming and the coherence factor in ultrasound imaging. IEEE Trans Ultrason Ferroelectr Freq Control. 2010;57:1329–46.
15. Kanai H, Sato M, Koiwa Y, et al. Transcutaneous measurement and spectrum analysis of heart wall vibrations. IEEE Trans Ultrason Ferroelectr Freq Control. 1996;43:791–810.
16. Mallart R, Fink M. Adaptive focusing in scattering media through sound-speed inhomogeneities: The van Cittert Zernike approach and focusing criterion. J Acoust Soc Am. 1994;96:3721–32.
17. Hverven SM, Rindal OMH, Rodriguez-Molares A, et al. The influence of speckle statistics on contrast metrics in ultrasound imaging. IEEE Ultrason Symp. 2017. https://doi.org/10.1109/ULTSYM.2017.8091949.
18. Hisatsu M, Mori S, Arakawa M, et al. Generalized coherence factor estimated from real signals in ultrasound beamforming. J Med Ultrasonics. 2020;47:179–92.
19. Hisatsu M, Mori S, Arakawa M, et al. Low-complexity generalized coherence factor estimated from binarized signals in ultrasound beamforming. J Med Ultrasonics. 2021;48:259–72.
20. Rindal OMH, Rodriguez-Molares A, Austeng A. The dark region artifact in adaptive ultrasound beamforming. IEEE Intl Ultrasound Symp. 2017. https://doi.org/10.1109/ULTSYM.2017.8092255.